Nonlinear Backstepping Controller for Magnetic Linked DC-DC Converter

Md. Rezaur Rahman Shipon, Md. Rashidul Islam, Md. Shahan Sarker, Md. Ashib Rahman, *Member, IEEE*, Waqas Hassan, *Senior Member, IEEE*, Md. Shazarul Islam, Md. Alamgir Hossain, *Senior Member, IEEE*

Abstract—This paper presents an advanced nonlinear backstepping controller for a magnetic-linked DC-DC converter, designed to achieve stable voltage regulation with zero steady-state error, minimal settling time, and reduced chattering effects. The controller's performance is evaluated under various operating conditions, including step changes in the reference signal, as well as variations in load and input voltage. The proposed controller features only a single adjustable gain parameter, which simplifies the overall design process. The performance of the controller is compared to that of the traditional proportionalintegral controller and other nonlinear sliding mode controllers, such as the double integral sliding mode controller and the no integral sliding mode controller. The results of simulations in MATLAB/Simulink demonstrate that the backstepping controller outperforms existing controllers in terms of overshoot, steadystate error, and settling time. Experimental validation on a scaleddown laboratory test platform further confirms the superior control performance of the proposed backstepping controller for magnetic-linked DC-DC converters.

Index Terms—Nonlinear backstepping controller, Magnetic linked dc-dc converter, Robust voltage regulation, Sliding mode controller.

I. Introduction

N recent years, renewable energy has achieved extensive attention due to the limitations of fossil fuels. In the case of the vast use of renewable energy and DC loads, DC microgrids are more compatible and reliable as there is no need for phase and frequency synchronization issues with the grid [1]. The conversion efficiency of the DC microgrid is also high because it reduces the energy conversion stages [2].

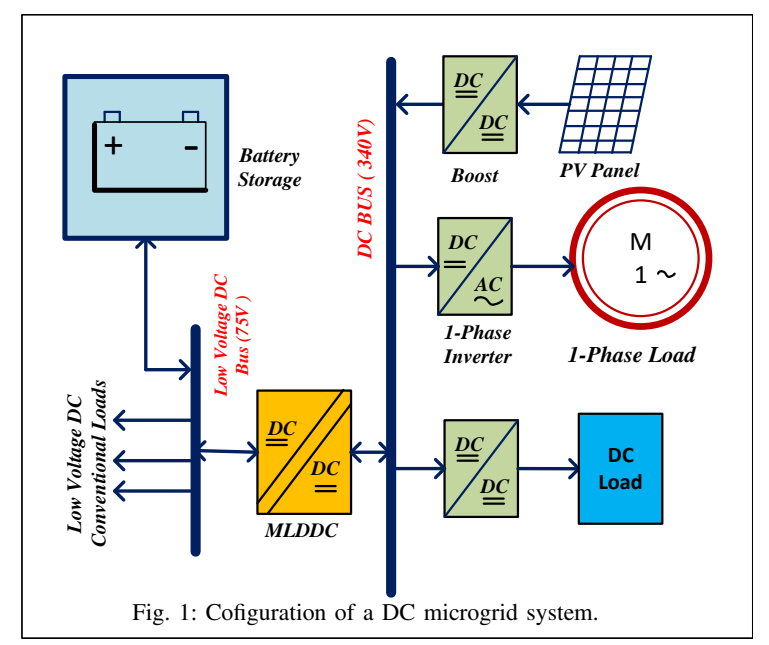
Bidirectional power transmission across several voltage levels in DC microgrids can be made possible by bidirectional magnetic-linked DC-DC converters (MLDDCs). Due to their several benefits, including galvanic isolation, simplicity of structure, high conversion ratio, and high efficiency [3], the MLDDCs are widely used in DC microgrid systems [4], [5], renewable energy conversion systems [6], battery storage systems [4], electric vehicles [7], [8], and solid-state transformers [9]. Fig. 1 shows a schematic of a DC microgrid

Md. Rezaur Rahman Shipon, Md. Rashidul Islam, Md. Shahan Sarker and Md. Shazarul Islam are with the Department of Electrical and Electronic Engineering, Rajshahi University of Engineering and Technology, Rajshahi 6204, Bangladesh (e-mail: shipon.r.eee@gmail.com; rashidul@eee.ruet.ac.bd; sarker.ruet.eee17@gmail.com; shazarulislam.ruet.eee16@gmail.com).

Md. Ashib Rahman is with Future Grids, APD Engineering, Melbourne, VIC 3006, Australia (e-mail: m.rahman.bd@ieee.org).

Waqas Hassan is with the School of Engineering, University of Tasmania, Hobart, Australia (e-mails: waqas.hassan@utas.edu.au).

Md. Alamgir Hossain is with the School of Engineering, University of Southern Queensland, Toowoomba, QLD 4350, Australia (e-mails: alamgir.hossain@unisq.edu.au).



system with battery storage based on MLDDC, DC-DC, and AC-DC converters. Depending on the operating mode, the MLDDC battery storage system based on the system may store or provide power. The designed controller for the MLDDC should also ensure high conversion efficiency, high power density, and high reliability of the MLDDC [3], [10], [11].

In order to provide galvanic isolation, dual-port MLDDCs are made up of two single- or three-phase bridges coupled by a high-frequency magnetic connection [12]. The three-phase topologies need complicated control schemes as well as for high-power applications. To reduce switching power losses, the MLDDCs with a high-frequency magnetic link, single or three-phase, can incorporate a resonant tank [13], although this calls for extra passive components. Thus, MLDDCs without resonant topologies are favored for applications that require high power density [13]. The power flow is primarily controlled by the phase shift between the voltage signals in two active bridges. The control method for the dual active bridge (DAB) can be classified into four types according to the control variables, which are single phase shift (SPS) control [14], extended phase shift (EPS) control [15], [16], dead phase shift (DPS) control [17]-[20] and triple phase shift (TPS) control [21]–[23]. Due to its simplicity in controlling active power through phase shift adjustment, the single phase shift (SPS) method is widely used [24].

The performance of the MLDCCs depends on the robustness of the closed loop feedback control strategy [4], and a number of linear and nonlinear controllers have been suggested to deal with this problem. Small signal analysis of the MLDDC

model was reported in [25] to suggest a conventional linear proportional-integral (PI) controller. However, the performance of the PI controller degrades when the operating point changes. This indicates that it cannot properly tune its gain values. A look-up table [26] based on nominal parameters of the MLDDC was used to create a gain scheduling strategy for the PI controller to solve this issue. As a result, parameter uncertainties may have an impact on the system performance.

Many nonlinear controllers have been suggested as well to overcome the problems and bandwidth constraints of linear controllers. Among them, the feedback linearization method, as suggested in [27], [28], is extremely dependent on an accurate system model, which in turn affects how well the controller performs. For the current control of MLDDC, a different controller known as a fuzzy logic controller (FLC) has been used [29]. Although no prior knowledge of the system data is necessary for the FLC, it depends on some estimated control variables, which need much tuning effort to map the output with the input perfectly. Additionally, there is no proper mechanism to demonstrate the FLC's close-loop stability [30]. Using a structural simplicity and performance comparable to other controllers, an artificial neural network-based controller for MLDDCs was suggested in [4].

In [28], the no integral sliding mode (NISM) controller for MLDDCs was presented. However, because there was no integral term in the control equation, it suffered from severe overshoot and steady-state error. Moreover, it is worth mentioning that the sliding mode controllers suffer from a chattering effect [31], [32]. Using integral terms in their control equations, controllers for single integral sliding mode (SISM) and double integral sliding mode (DISM) controllers, as described in [32], considerably decreased steady-state error. However, these controllers come with their own complexities. Specifically, the SISM and DISM controllers require the tuning of three and four adjustable gains, respectively, making the tuning process more complex and analytically demanding.

The backstepping controller is favored over conventional sliding mode controllers (SMCs) for MLDDCs because of its continuous control input, which is essential for phase shift modulation in DAB converters. Unlike SMCs, the backstepping approach eliminates chattering, improves robustness, and simplifies tuning by requiring only a single gain parameter, thus improving efficiency and practicality in power electronics applications [32].

To overcome these issues and address the challenges posed by system nonlinearities, the same authors proposed a nonlinear backstepping controller (BSC) in [33]. This controller is particularly well-suited for MLDDCs because it efficiently handles nonlinearities with only one adjustable gain parameter, in contrast to traditional sliding mode and proportional-integral controllers that often require complex multi-gain tuning. Furthermore, the design inherently mitigates chattering, overshoot, and steady-state errors [34], [35].

Moreover, the proposed BSC provides a foundational framework that can be adapted to control other DC-DC converter topologies, particularly those involving bidirectional power transfer and high-frequency magnetic links. By tailoring the mathematical model to the specific characteristics of alter-

native converter architectures, this approach offers promising potential for broader applications in renewable energy systems and grid-connected converters [3].

This paper is extended by including experimental results to validate the simulation performance of the proposed BSC. In addition, the performance of the proposed BSC is tested under different operating conditions. Furthermore, the superior performance of the proposed controller compared to existing controllers is quantitatively compared and presented in a more comprehensive manner.

This research offers the following key contributions:

- The study presents a mathematical model of nonlinear BSC that is especially tailored for MLDDC. In order to overcome the shortcomings of current control techniques, the proposed BSC provides better stability and voltage regulation throughout a range of operating situations.
- 2) The nonlinear BSC for MLDDCs proposed in this study provides continuous phase-shift modulation, removes chattering, improves resilience, and is easy to tune using a single gain parameter.
- The proposed BSC is thoroughly compared to the nonlinear sliding mode controllers that are currently in use, such as PI, NISM, and DISM controllers; and
- 4) The practical usefulness of the proposed BSC is confirmed by experimental validation.

The following is the structure of this article: In section 1, bidirectional magnetic linked DC-DC converters and their uses are introduced along with a thorough literature assessment. The controller design and the dual-port MLDDCs circuit architecture are described in depth in Section 2. In Section 3, the analysis and the results of the simulation are presented. In Section 4, the analysis and results of the experiment are covered. The research contributions and consequences based on the findings are summarized in Section 5, which concludes the paper.

II. METHODOLOGY

A. THE CONFIGURATION

1) Circuit Configuration of the Dual-port MLDDC: Fig. 2 illustrates the circuit design of the dual-port MLDDC. A high-frequency magnetic connection links the two active bridges H_1 and H_2 , using magnetic coupling. The circuit includes an equivalent inductance (L_s) , an equivalent resistance (R_s) , two capacitors (C_s, C_{dc}) , a smoothing inductor (L_f) and its internal resistance (R_f) . An auxiliary inductance can be added to achieve the desired output power [3]. The low-voltage battery connected to the high-frequency transformer on the primary side is represented by H_1 , while the high-voltage DC bus connected to the secondary side is represented by H_2 . The C_{dc} smoothing capacitors emulate the magnetic connection.

To achieve a smooth current, the input inductor (L_s) is used. The equivalent inductance (L_s) is composed of the winding leakage inductance and additional inductance on the secondary side, given as $L_s = L_a + n^2 L_{LV} + L_{HV}$. Here, L_{LV} and L_{HV} denote the winding leakage inductances, and L_a represents the additional inductance responsible for regulating the power of the MLDDC.

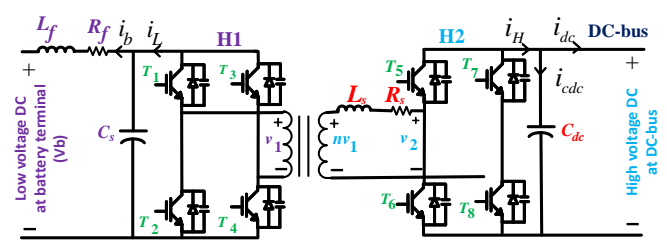


Fig. 2: Configuration of a dual-port MLDDC.

The equivalent resistance (R_s) is the sum of two resistances, expressed as $R_s = R_a + n^2 R_{LV} + R_{HV}$. Here, R_{LV} and R_{HV} represent the internal resistances of the magnetic connection, R_a denotes the resistance of the additional inductance, and n is the transformer turn ratio.

This research focuses on the control of an isolated bidirectional dual-active-bridge (DAB) DC-DC converter, where the low-voltage (LV) side of the DAB converter is connected to the battery, and the high-voltage (HV) side is connected to the DC bus. The operation of the DAB converter is governed by the higher-level controller of the system [36].

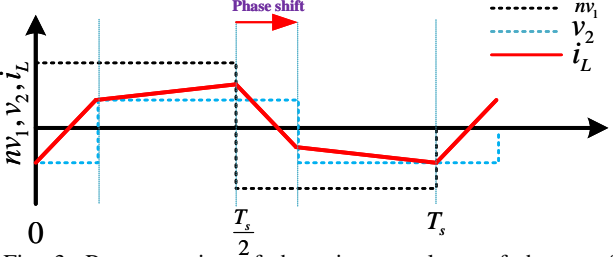


Fig. 3: Representation of the primary voltage of the transformer referred to as secondary (nv_1) and the voltage at the terminal of H_2 the bridge (v_2) and the corresponding inductor current.

2) Operation of the dual-port MLDDC: Fig. 3 shows the MLDDC voltages at both ends of the analogous inductor and the current flowing through the inductor for single phase-shift modulation (SPSM). A positive phase-shift ratio in this illustration means that the voltage in the primary (v_1) with respect to the secondary is higher than the voltage (v_2) . The phase difference and magnitudes of the voltages (nv_1, v_2) at the two ends of the inductor determine the forms of the current and voltage.

The average power (P_{out}) delivered can be expressed as follows [32], [37]:

$$P_{out} = \frac{n|v_1||v_2|}{2fL_s} \frac{\delta(\pi - \delta)}{\pi^2} = \frac{n|v_1||v_2|}{2fL_s} d(1 - d)$$
 (1)

Equation (1) indicates that the voltages $(n|v_1|,|v_2|)$ the phase shift angle (δ) or the phase shift ratio (d), the equivalent inductance $((L_s))$ and the switching frequency (f) determine the magnitude and direction of power flow if dead time and power losses in semiconductor devices are not taken into account. This is where the power for the bridge comes from, producing the voltage that leads to the square wave. Power will be transferred to the DC bus from the battery side in the event of a positive phase change. If there is a negative phase shift, the direction of power flow will be reversed.

3) Dynamic Equations of the Output Voltage and Current: A low-frequency harmonic model can be created for the output voltage and current of the dual-port MLDDC for the SPSM

[26], based on the Fourier series of the switching function. The dynamic equation for the output voltage of the MLDDC can be derived as follows:

$$\frac{dv_{dc}}{dt} = -\frac{8}{C_{dc}\pi^2} \sum_{k=1,3,5,\dots}^{\infty} \frac{\cos\{\phi_z(k)\}\}}{k^2 |Z(k)|} v_{dc} + \frac{8}{C_{dc}\pi^2} \sum_{k=1,3,5,\dots}^{\infty} \frac{\cos\{k\delta - \phi_z(k)\}\}}{k^2 |Z(k)|} nv_b(t) - \frac{i_{dc}}{C_{dc}} \quad (2)$$

The expression for the output current equation can be presented as:

$$\frac{di_b}{dt} = -\frac{R_f}{L_f} i_b + \frac{8}{L_f C_s} \sum_{k=1,3,5,\dots}^{\infty} \frac{\sin(\delta - \phi_z(k))}{\pi^2 |Z(k)|} \frac{v_{dc}}{n} - \left(\frac{1}{L_f} + \sum_{k=1,3,5,\dots}^{\infty} \sin(\phi_z(k))\right) v_b \quad (3)$$

where

$$|Z(k)| = \sqrt{R_s^2 + (k\omega_s L_s)^2} \tag{4}$$

and

$$\phi_z(k) = \tan^{-1}\left(\frac{k\omega_s L_s}{R_s}\right) \tag{5}$$

here ω_s represents the switching frequency in rad/s, k denotes the harmonic order (k=1,3,5,...), and |Z(k)| and $\phi_z(k)$ represents the phase angle and impedance between the two active bridges of the MLDDC, respectively. Due to the robustness of the BSC and SMCs, in this study only the fundamental harmonic component (k=1) is taken into account [34], [35], [38].

B. CONTROLLERS DESIGN

In this part, the controller design process is described, which identifies the phase-shift ratio (d) and the required phase-shift angle (δ) . Using Lyapunov stability theory, the stability of the systems is examined. Assuming the following for the system with a disturbance (E):

$$\frac{dv_{dc}}{dt} = \dot{v}_{dc} = \alpha(v_{dc}) + \beta \cdot u + E \tag{6}$$

where u is designated as a new control input and is a function of δ in the manner described below. The two non-linear functions are α and β .

$$u = \cos(\delta + \delta_0 - \phi_z(1)) \tag{7}$$

In this case, $\phi_z(1)$ at the switching frequency is found from (5). In light of (2) and (6), it follows that:

$$\alpha(v_{dc}) = -\frac{8}{C_{dc}\pi^2} \frac{\cos(\phi_z(1))}{|Z(1)|} v_{dc}$$
 (8)

$$\beta = \frac{8}{C_{dc}\pi^2} \frac{nv_b}{|Z(1)|} \tag{9}$$

Considering the load current effect as a disturbance, then:

$$E = -\frac{i_{dc}}{C_{dc}} \tag{10}$$

Considering $\delta_0 - \phi_z(1) = \frac{\pi}{2}$ in (7):

$$u = \sin(\delta^*) \tag{11}$$

where δ^* is the phase shift angle reference.

1) Design of the Proposed Backstepping Controller: Considering only the state of the voltage condition for which the tracking error *e* is computed and represented as [39]:

$$e = v_{dc} - v_{dc_{\text{(ref)}}} \tag{12}$$

where the output voltage reference value is $v_{dc_{ref}}$. Just differentiating (12) yields the following error dynamic equation:

$$\dot{e} = \dot{v}_{dc} - \dot{v}_{dc_{\text{(ref)}}} \tag{13}$$

By inserting \dot{v}_{dc} from (2) into equation (12), the following can be deduced:

$$\dot{e} = -\frac{8}{C_{dc}\pi^2} \frac{\cos\{\phi_z(1)|Z(1)|\}}{v_{dc}} + \frac{8}{C_{dc}\pi^2} \frac{nv_b}{|Z(1)|} \sin \delta^* - \frac{i_{dc}}{C_{dc}} - \dot{v}_{dc_{(ref)}}$$
(14)

A stable system dynamic is achieved by computing the phase-shift angle δ in such a way that $(i.e., e \to 0 \text{ as } t \to \infty)$. The system energy function may be described as follows using the Lyapunov stability theorem:

$$W = \frac{1}{2}e^2 \tag{15}$$

Once the derivative of (15) is calculated, it may be expressed as $\dot{W} = e\dot{e}$ (16)

When the value of e is changed from (14) to (16), the result is as follows:

Hows:

$$\dot{W} = e \left\{ -\frac{8}{C_{dc}\pi^2} \frac{\cos(\phi_z(1))}{|Z(1)|} v_{dc} + \frac{8}{C_{dc}\pi^2} \frac{nv_b}{|Z(1)|} \sin \delta^* - \frac{i_{dc}}{C_{dc}} - \dot{v}_{dc_{(ref)}} \right\}$$
(17)

Lyapunov's theory states that the system can only be considered asymptotically stable if and only if $\dot{W} < 0$. If (18) turns out to be true, then this condition can hold.

$$-\frac{8}{C_{dc}\pi^{2}} \frac{\cos(\phi_{z}(1))}{|Z(1)|} v_{dc} + \frac{8}{C_{dc}\pi^{2}} \frac{nv_{b}}{|Z(1)|} \sin \delta^{*} - \frac{i_{dc}}{C_{dc}} - \dot{v}_{dc_{(ref)}} = ke \quad (18)$$

where k is a negative constant that determines the convergence rate of error. With this, (17) can be modified as:

$$\dot{W} = ke^2 \tag{19}$$

From (19), it can be deduced that the system is asymptotically stable according to the stability condition. From (18), the reaching law can be written as follows:

$$\sin \delta^* = \left[\left(\frac{C_{dc} \pi^2}{8} \right) \frac{|Z(1)|}{nV_b} \right]$$

$$\times \left[\left(\frac{8}{C_{dc} \pi^2} \right) \frac{\cos(\phi_z(1))}{|Z(1)|} V_{dc} + \frac{i_{dc}}{C_{dc}} + \dot{v}_{dc_{(ref)}} + ke \right]$$
(20)

$$\delta^* = \sin^{-1} \left[\beta^{-1} \left(\alpha(V_{dc}) + E + \dot{v}_{dc_{(ref)}} + ke \right) \right] \tag{21}$$

The gain k < 0 ensures asymptotic stability ($\dot{W} = ke^2 < 0$), with |k| tuned to balance convergence rate, avoid control saturation ($|\sin(\delta^*)| \le 1$), and reject disturbances. Robustness is validated under $\pm 10\%$ and $\pm 25\%$ parametric variations. The formula for calculating the phase-shift ratio (d^*) is as follows:

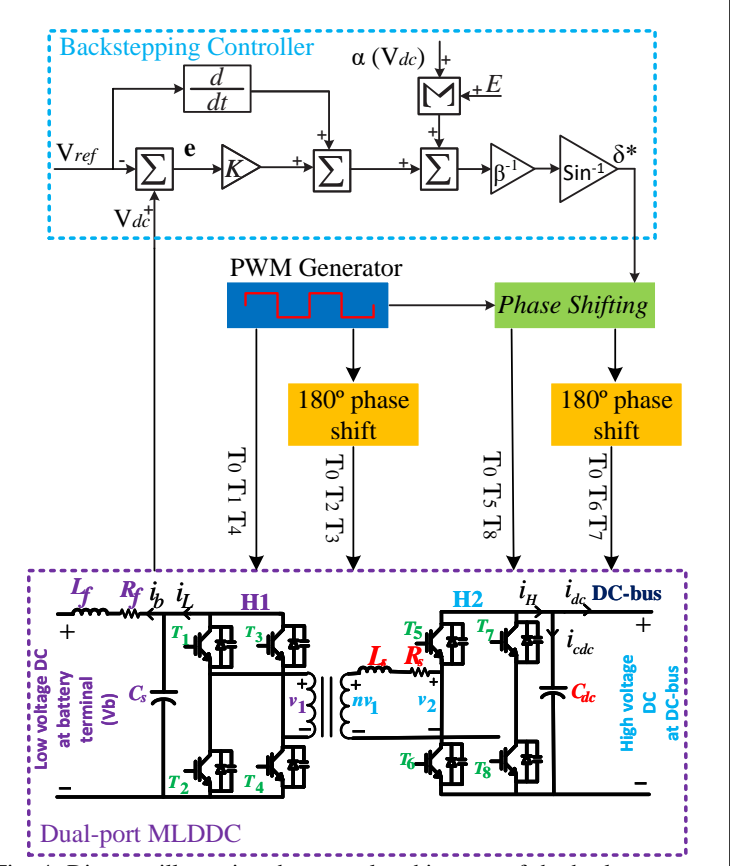


Fig. 4: Diagram illustrating the control architecture of the backstepping controller developed for the dual-port magnetically coupled DC-DC converter.

TABLE I: Simulation model parameters of the MLDDC.

Parameters	Values
Rated output power (Pout)	1415 W
LV side voltage (Vb)	75 V
HV side voltage (Vdc)	340 V
Transformer turn ratio (n)	$4.53 \ (\approx 340/75)$
Equivalent series inductance referred to	1.02 mH
secondary side $((L_s)$	
Capacitance (Cdc)	600 μF
Primary-side dc inductance $((L_f)$	16 μΗ
Sampling / switching frequencies (f)	100 kHz

$$d^* = \frac{\delta^*}{\pi} \tag{22}$$

The suggested BSC controller created for the MLDDC is depicted in Fig. 4, which is the control block diagram. T1, T2, T3, and T4 are the four IGBTs that make up the first active bridge H1, whereas T5, T6, T7, and T8 make up the second active bridge H2. A phase-shifted version of the PWM signal directed towards the H1 bridge powers the H2 bridge via an input signal. Equations (21) and (22) are utilized by the BSC controller to determine the phase-shift amount.

Double integral sliding mode control (DISMC) was chosen over simple integral sliding mode control (ISMC) because it is better able to handle higher-order uncertainties, reduce TABLE II: Controller gain parameters.

Controllers	Parameters	Values
PI	k_P, k_I	0.015, 0.50
NISM	k_{NI}, μ_{NI}	$1, 1 \times 10^3$
DISM	$k_1, k_2, k_{DI}, \mu_{DI}$	1.08×10^3 , 1×10^{-30} ,
		$1 \times 10^{-12}, 20 \times 10^3$
BSC	k	-15×10^{3}

steady-state errors, and improve convergence rates in complex dynamic systems. Consequently, DISMC is considered a more suitable option for the system under investigation. In addition, since the design procedure for sliding mode control is nearly identical to that of the proposed BSC, a brief description of the SMC design is provided here.

2) Design of the Sliding Mode Controller: The sliding surface for NISMC and DISMC be defined as follows [31], [32]:

$$S_{NI} = e (23)$$

$$S_{DI} = e + k_1 \int e \, dt + k_2 \int \int e \, dt \, dt \qquad (24)$$

let the Lyapunov energy functions for NISMC and DISMC be

$$W_{NI} = \frac{1}{2} S_{NI}^2 \tag{25}$$

$$W_{DI} = \frac{1}{2}S_{DI}^2 \tag{26}$$

Taking the derivative of Eqn. (25) and (26), we obtain:

$$\dot{W}_{NI} = S_{NI} \left(\alpha(V_{dc}) + \beta u + E - \dot{V}_{dc(ref)} \right)$$
 (27)

$$\dot{W}_{DI} = S_{DI} \left(\alpha(V_{dc}) + \beta u + E - \dot{V}_{dc(ref)} + k_1 e + k_2 \int e \, dt \right)$$
 (28)

Let,

$$\alpha(V_{dc}) + \beta u + E - \dot{V}_{dc(ref)} = -k_{NI}\beta \operatorname{sign}(S_{NI})$$
 (29)

$$\alpha(V_{dc}) + \beta u + E - \dot{V}_{dc(ref)} + k_1 e + k_2 \int e \, dt$$

$$= -k_{DI} \beta \operatorname{sign}(S_{DI}) \quad (30)$$

where generally the signum function is defined as $sign(S) = \frac{|S|}{S}$. Now, putting Eqn. (29) and (30) to Eqn. (27) and (28) respectfully, the following terms are obtained:

$$\dot{W}_{NI} = -k_{NI}\beta |S_{NI}| \tag{31}$$

$$\dot{W}_{DI} = -k_{DI}\beta|S_{DI}|\tag{32}$$

From Eqn. (31) and (32), it can be deduced that both DISMC and NISMC will be asymptotically stable if and only if k_{NI} , k_{DI} and β is positive. Now, from (29) and (30) following control inputs are obtained:

$$u_{NI} = -\beta^{-1} \left(\alpha(V_{dc}) + E - \dot{V}_{\text{dc(ref)}} \right) - k_{NI} \text{sign}(S_{NI})$$
 (33)

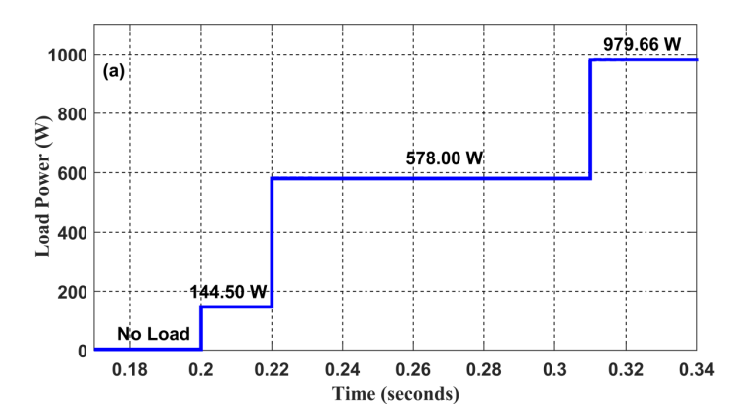
$$u_{DI} = -\beta^{-1} \left(\alpha(V_{dc}) + E - \dot{V}_{dc(ref)} + k_1 e + k_2 \int e \, dt \right) - k_{DI} \operatorname{sign}(S_{DI}) \quad (34)$$

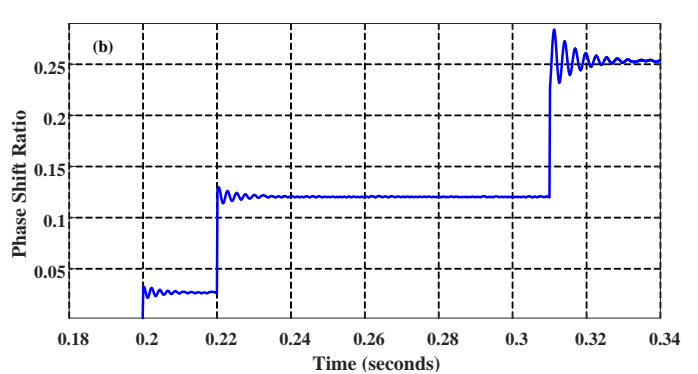
Replacing the "sign" function with a hyperbolic tangent (tanh) function to obtain a smooth control signal in equations (33) and (34), from equation (11) the control input can be found as:

$$\delta_{NI}^* = -\sin^{-1} \left[\beta^{-1} \left(\alpha(V_{dc}) + E - \dot{V}_{dc(ref)} \right) + k_{NI} \tanh \left(\frac{S_{NI}}{\mu_{NI}} \right) \right]$$
(35)

$$\delta_{DI}^* = -\sin^{-1} \left[-\beta^{-1} \left(\alpha(V_{dc}) + E - \dot{V}_{\text{dc(ref)}} + k_1 e + k_2 \int e \, dt \right) + k_{DI} \tanh \left(\frac{S_{DI}}{\mu_{DI}} \right) \right]$$
(36)

where μ_{NI} and μ_{DI} are two constants, which determine the boundary layer k_1 , k_2 , k_{NI} and k_{DI} are positive constants.





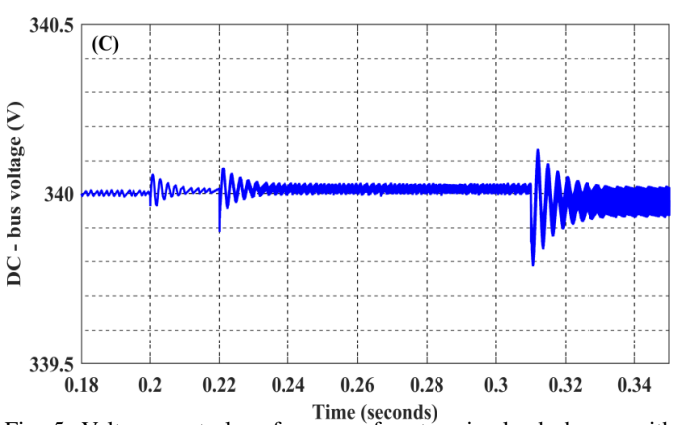


Fig. 5: Voltage control performance for stepwise load change with the proposed BSC: (a) load power, (b) phase-shift ratio and (c) dc-bus voltage.

III. SIMULATION RESULTS AND ANALYSIS

The performance of the proposed BSC is evaluated in MATLAB/Simulink and compared to PI, NISM and DISM controllers. As mentioned earlier in our paper, our proposed BSC controller consists of only one gain parameter, k. From equation (19) in our manuscript, the value of k needs to be negative to make the system asymptotically stable according to

the Lyapunov stability theory. According to this condition, the value of k has been selected by trial and error considering minimal overshoot, the smallest transients and the lowest settling times. As the BSC needs only one gain parameter, it is very easy to tune practically. The system parameters and controller gains that provide the best performance are listed in Table I and Table II, respectively.

The effectiveness of the suggested BSC is shown in Fig. 5(a) for various loads, such as 144.50 W, 578.00 W, and 979.66 W. The controller can monitor the reference voltage extremely well under all working conditions, as Fig. 5(c) demonstrates, with the exception of a very low fluctuation of 0.0018%. Here, the phase shift ratio is positive because the power is transferred from the LV side to the HV side, as shown in Fig. 5(b).

TABLE III: Comparative analysis between controllers

Variation	Performance		Control strategy			
Para -meters		Metrics	NISMC	DISMC	PI	BSC
	DC-bus	Settling time (t/ms)	71.5	71.4	90.4	71.2
	voltage	Overshoot (%)	3.08	2.76	3.39	2.17
Load		Undershoot (%)	0	0	2.43	0
Loau		Steady-state error (%)	0.035	0.027	0.100	0.021
	Inductor	Settling time (t/ms)	400.0	393.4	402.5	373.2
	current	Overshoot (%)	88.26	30.03	91.02	23.38
		Undershoot (%)	87.86	30.29	94.05	24.67
		Steady-state error (%)	0.173	0.095	0.306	0.085
Reference	DC-bus	Settling time (t/ms)	211.0	210.6	305.4	210.4
voltage	voltage	Overshoot (%)	16.84	16.29	58.36	15.91
		Undershoot (%)	0	0	24.37	0
		Steady-state error (%)	0.029	0.019	0.501	0.015
Input	DC-bus	Settling time (t/ms)	82.1	73.0	98.7	66.5
voltage	voltage	Overshoot (%)	2.96	2.95	2.73	1.98
		Undershoot (%)	2.62	1.03	2.33	0
		Steady-state error (%)	0.004	0.006	0.059	0.001

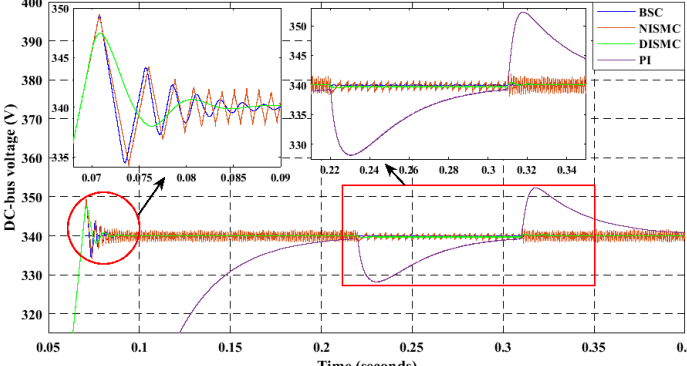


Fig. 6: Comparisons of voltage control performance for a sudden load change.

Fig. 6 compares the voltage control under abrupt load changes using the proposed BSC with PI, NISM, and DISM controllers. The figure shows that the PI controller exhibits considerable transient behavior, with higher settling time (90.4 t/ms), overshoot (3.39%), undershoot (2.43%) and stedy-state error (0.1%), indicating its inability to properly track the

voltage during 0.22 ms under sudden load changes. Therefore, the PI controller is excluded from further comparisons. NISM reduces chattering by adjusting k or increasing μ , but this results in longer settling times and increased steady-state error. Controller gains were selected for the lowest settlement times, minimal overshoot, and smallest transients. DISM shows a steady-state error of 0.027% with good transient response and no chattering. Although BSC has a slightly higher start-up overshoot than DISMC; it requires only one gain parameter versus the three- and integral action of a DISMC. However, the proposed BSC outperforms both NISM and DISM, achieving a steady-state error of 0.021%, a shorter settling time (71.2 ms), and lower overshoot (2.17%).

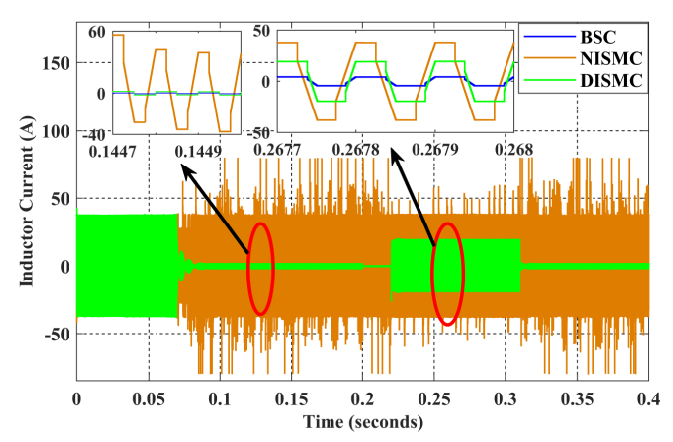


Fig. 7: Comparisons of equivalent inductor currents for a sudden load change with the proposed BSC and existing NISMC and DISMC.

Fig. 7 shows the inductor currents for different controllers. The NISM controller consistently exhibits chattering during a sudden load change between 0.2675 s and 0.2682 s. The DISMC and BSC show lower chattering issues, but the inductor current is much higher in the DISMC than in the BSC. This results in a slower steady-state error of 0.085% compared to DISM and NISM, indicating a lower design cost for the BSC. Table III shows that for abrupt load variations, the BSC has a shorter settling time (373.2 ms), less overshoot (23.38%) and less undershoot (24.67%) compared to existing DISM and NISM controllers.

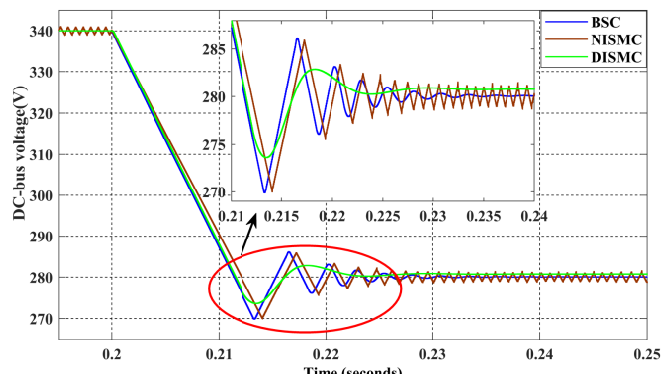


Fig. 8: Voltage control performance at changing the reference voltage.

Fig. 8 shows a sudden change in the reference voltage from 340 V to 280 V at 0.2 s. The NISM controller exhibits significant chattering with a 16.84% overshoot, while the DISM controller has a lower overshoot (16.29%) but a 0.13%

steady-state error. However, the proposed BSC performs both with 0.015% steady-state error, shorter settling time (210.4 ms) and less overshoot (15.91%).

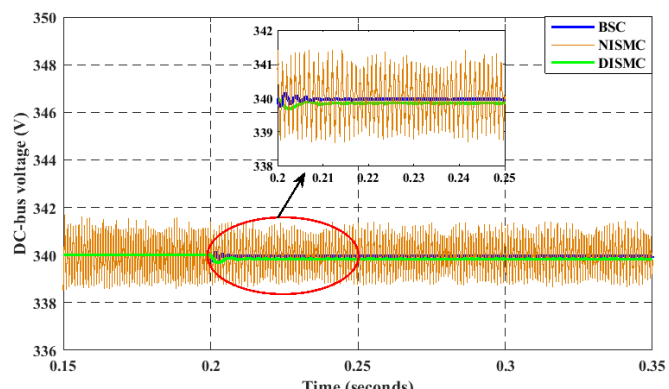


Fig. 9: Voltage control performance when the input voltage is changed.

Fig. 9 illustrates the change in the input voltage of 30% at 0.2 s to compare the control performances of the BSC, NISM, and DISM controllers. The DISM controller shows less chattering than the NISM controller but struggles with reference voltage tracking. However, the proposed BSC demonstrates superior performance with 0.001% steady-state error, shorter settling time (66.5 ms) and lower overshoot (1.98%).

The performance metrics in Table III compare the PI, DISMC, BSC and NISMC controllers based on variations in DC-bus voltage, inductor current, reference voltage and input voltage.

To evaluate the robustness of the proposed nonlinear BSC for the MLDDC, a parametric uncertainty analysis is performed. In practical scenarios, variations in the transformer turn ratio (n), equivalent series inductance (L_s) , and DC-link capacitance (C_{dc}) of the dual-port MLDDC can arise due to manufacturing tolerances, temperature fluctuations, or component aging. This analysis examines the BSC's inherent capability to manage such uncertainties using a single gain parameter, while ensuring system stability through a Lyapunov-based framework.

The nominal parameters listed in Table I (n = 4.53, $L_s = 1.02 \,\mathrm{mH}, \ C_{dc} = 600 \,\mathrm{\mu F})$ were perturbed by $\pm 10\%$ and $\pm 25\%$ within the BSC control law to evaluate robustness. The resulting DC-bus voltage response was analyzed by measuring key performance indicators, including settling time, overshoot, undershoot, and steady-state error. The results are summarized in Table IV and illustrated in Fig. 10. For variations in the transformer turn ratio (n), as shown in Fig. 10(a), the output voltage successfully tracks the reference of 340 V, with settling times below 75 ms and steadystate errors ranging from 0.021% under nominal conditions to a maximum of 0.035% at a +25% deviation. Inductance variations (L_s) , presented in Fig. 10(b), result in a modest increase in overshoot, reaching approximately 2.85% at +25% variation, while overall system stability is preserved. Changes in the DC-link capacitance (C_{dc}) , illustrated in Fig. 10(c), exhibit minimal influence on system performance, with steadystate errors remaining below 0.030% and settling times under 72.3 ms. These results demonstrate that, despite parametric

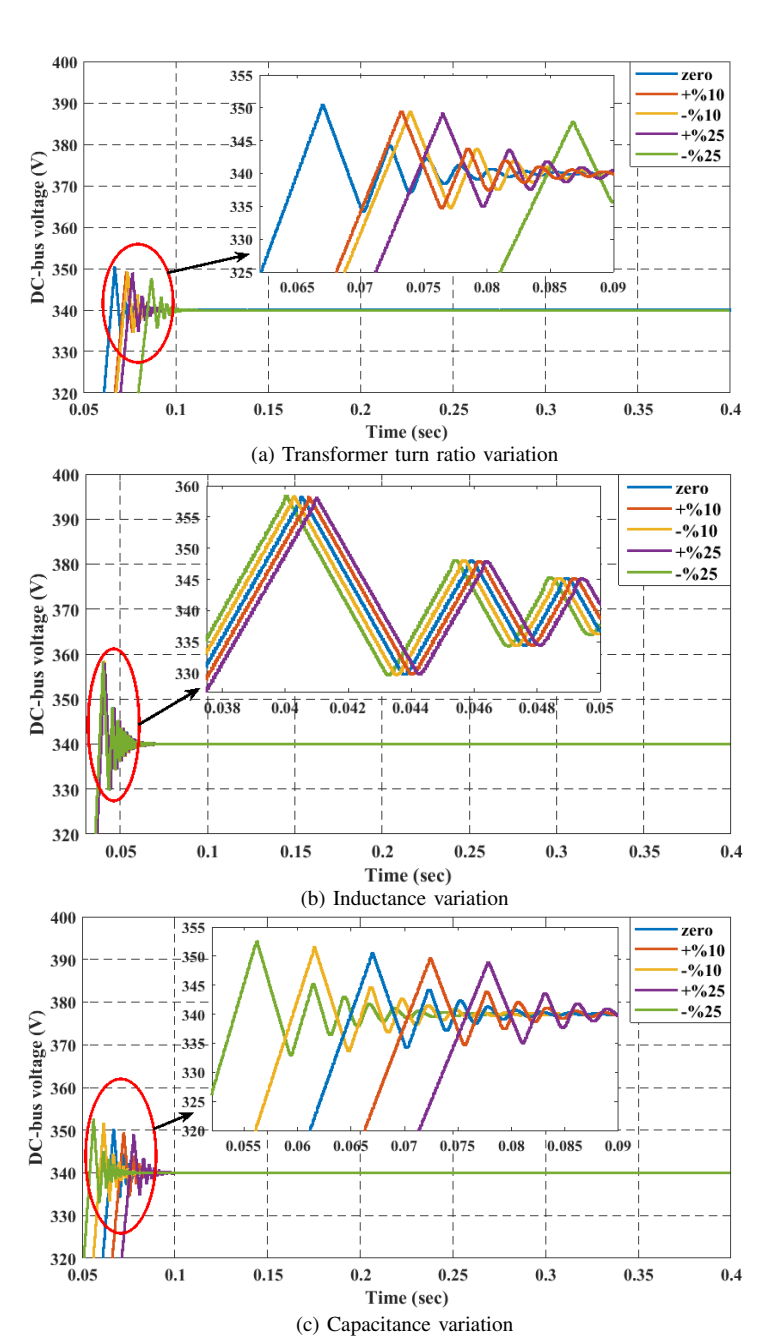


Fig. 10: DC-bus voltage response under parametric uncertainty: (a) transformer turn ratio (n), (b) inductor (L_s) , and (c) capacitor (C_{dc}) . uncertainties, the proposed nonlinear BSC effectively regulates the output voltage and reliably brings the system to the desired stable operating point.

IV. EXPERIMENTAL RESULTS

A prototype of a bidirectional MLDDC, as shown in Fig. 11, is built to verify the effectiveness of the advanced non-linear BSC proposed. The rated voltage on the low-voltage side is 50 V, while the DC bus voltage is 150 V. The experimental setup consists of Imperix power modules, a DC power supply, an electronic DC load, Imperix B-Box RCP, and magnetic components to test the control scheme. Experimental results were obtained using Imperix Cockpit software, a robust real-time monitoring and control tool specifically designed for power electronics systems. The proposed controller relies

TABLE IV: Parametric uncertainty analysis results

Parameter	Variation	Settling Time (ms)	Overshoot (%)	Steady-State Error (%)
	Nominal	71.2	2.17	0.021
	+10%	72.5	2.20	0.025
Transformer Ratio (n)	-10%	72.0	2.25	0.024
	+25%	74.8	2.52	0.035
	-25%	74.5	2.55	0.032
	Nominal	71.2	2.17	0.021
	+10%	73.0	2.40	0.028
Inductor (L_s)	-10%	72.8	2.35	0.027
	+25%	75.5	2.85	0.038
	-25%	75.2	2.80	0.036
Capacitor (C_{dc})	Nominal	71.2	2.17	0.021
	+10%	71.8	2.20	0.023
	-10%	71.5	2.18	0.022
	+25%	72.3	2.25	0.030
	-25%	72.0	2.22	0.028

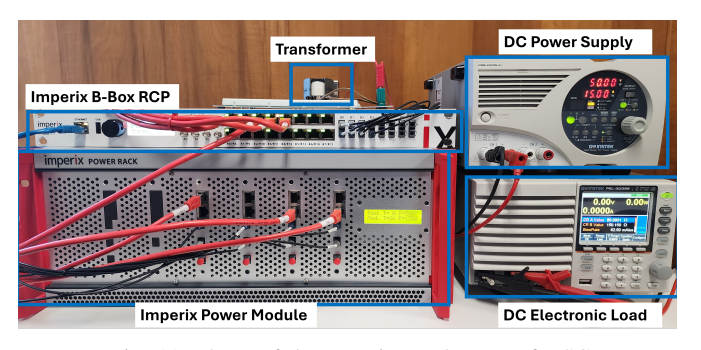


Fig. 11: Photo of the experimental setup of BSC.

solely on standard, readily available measurements (input and output voltages, inductor current) and does not require any additional sensors or specialized hardware beyond what is typically required in conventional converter control schemes. The parameters of the experimental setup are presented in Table V.

Fig. 12 illustrates the output voltage response of the BSC during a step load increase from 150 W to 250 W at 0.1 s. The DC bus voltage remains well regulated at 150 V, exhibiting minimal chattering and a small overshoot of 0.23%. The steady-state error is also very low, at 0.1%.

The BSC for the MLDDC output DC bus voltage is shown in Fig. 13 after an abrupt load drop from 250 W to 150 W at 0.1 s. With only slight chattering and an overshoot of 0.80%, the output voltage is well regulated.

The BSC voltage tracking performance for a sudden change in reference DC bus voltage is shown in Fig. 14 and Fig. 15. Fig. 14 displays the output DC bus voltage for a sudden increase in reference voltage from 150 V to 175 V, while

TABLE V: Experimental Model Parameters of the MLDDC.

Parameters	Values
Rated output power (Pout)	250 W
LV side voltage (Vb)	50 V
HV side voltage (Vdc)	150 V
Transformer turn ratio (n)	$0.25 \ (\approx 1:4)$
Equivalent series inductance referred to	47 μΗ
secondary side (L)	
Capacitance (Cdc)	470 μF
Primary-side dc inductance (Ls)	55 μH
Sampling / switching frequencies (f)	100 kHz
Backstepping controller gain parameter (K)	-8000

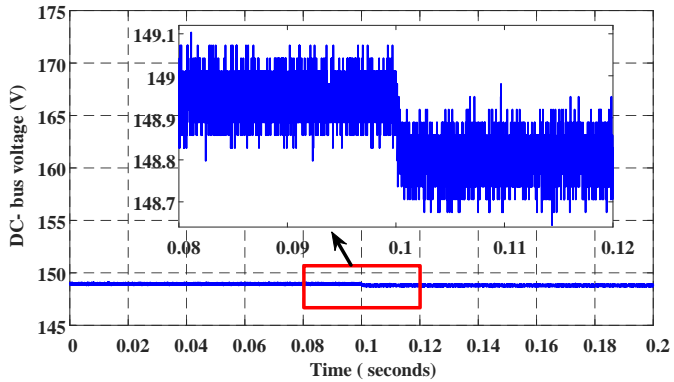


Fig. 12: Experimental waveforms showing the step-up in load variation from 150 W (140 ohms) to 250 W (90 ohms) using the BSC.

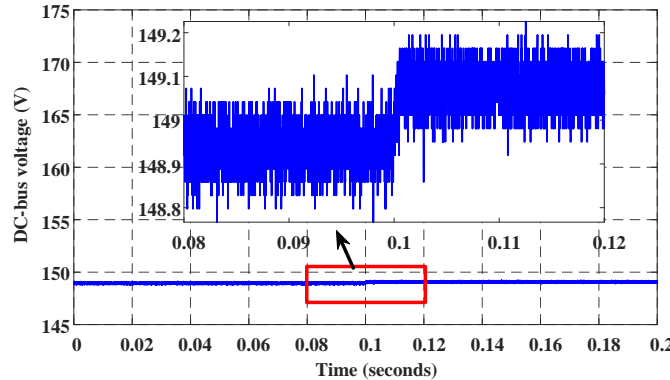


Fig. 13: Experimental waveforms with step-down in load from 250 W (90 ohms) to 150 W (140 ohms) using the BSC.

Fig. 15 shows the response to a decrease in reference voltage from 150 V to 125 V. In both cases, the proposed controller effectively tracks the reference voltage within a very short time period, specifically 6.20 ms and 7.36 ms, respectively.

The dynamic performance of the proposed controller (BSC) in response to a change in input voltage is depicted in Fig. 16. The input battery voltage suddenly decreases from 50 V to 40 V at 0.04 seconds. The BSC voltage tracking capabilities show excellent reference DC bus voltage following, with only minor chattering and a minimal steady-state error of 0.4%. The experimental output performance parameters are summarized in Table VI.

TABLE VI: Experimental result performance

Variation	Control strategy	Changing time (t/s)	Performance metrics		
	strategy	unie (us)	Settling time (t/ms)	Over- shoot(%)	Under- shoot(%)
Load	Increasing	0.1	0	0.23	0
Load	Decreasing	0.1	0	0.80	0
Reference	Increasing	0.05	6.20	0.11	0
voltage	Decreasing	0.05	7.36	20.07	0
Input voltage	-	0.04	0	0.54	0

The voltage waveform serves as a key performance indicator, encapsulating the controller's ability to maintain system stability and regulate output under dynamic conditions. Since voltage deviations directly correlate with system disturbances, analyzing their response provides reliable validation of the controller's effectiveness. Experimental results confirm that the proposed BSC effectively regulates the DC bus voltage, ensuring stability, transient suppression, and dynamic adaptability.

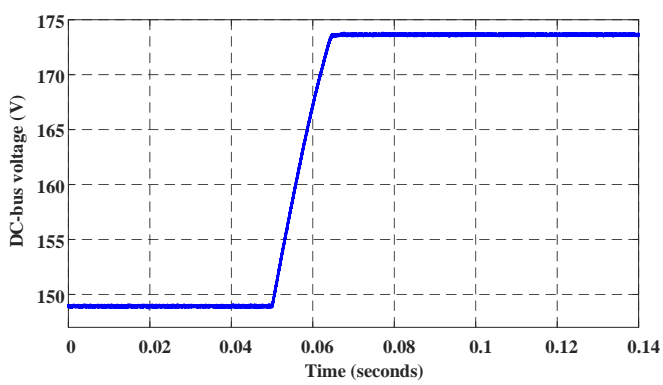


Fig. 14: Experimental waveforms showing the response to a step-up voltage reference from 150 V to 175 V using the BSC.

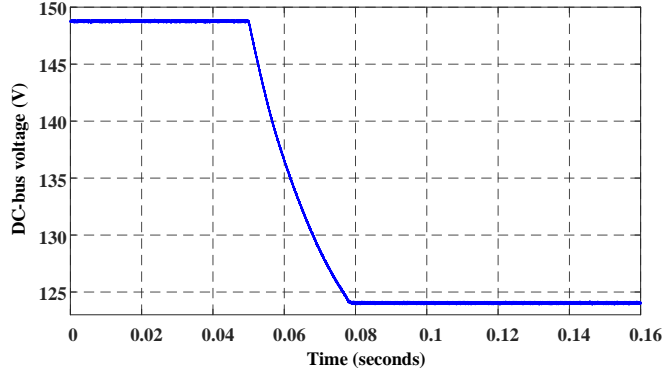


Fig. 15: Experimental waveforms for a step-down voltage reference transition from 150 V to 125 V using a BSC.

The strong correlation between simulation and experimental findings further reinforces that the dynamic phase shift ratio of the BSC and the current waveforms align with the theoretical predictions in Table III. Additionally, the proposed bidirectional MLDDC controller demonstrates exceptional performance in various dynamic scenarios, including abrupt load changes and sudden variations in reference and input voltages. It ensures robust voltage regulation with minimal chattering and overshoot. Fast response times in voltage tracking tests, combined with low steady-state errors, further validate the efficacy of the controller, confirming its ability to maintain stable and reliable operation under various conditions.

V. Conclusion

In this paper, a non-linear backstepping controller (BSC) for a magnetic-linked DC-DC converter (MLDDC) is proposed. The controller is designed based on the nonlinear dynamic model of the MLDDC, which is developed using the Fourier series of the switching function. The performance of the BSC is evaluated by simulation and compared with existing controllers such as PI, NISMC, and DISMC under various conditions. The BSC tracks the reference voltage with the smallest fluctuation. A comparative analysis during a sudden load change (144.5 W to 903.13 W) demonstrates that the BSC outperforms other controllers with an overshoot of 2.17% (compared to 2.76% for DISMC, 3.08% for NISMC, and 4.38% for PI) and a steady-state error of 0.021% (compared to 0.027% for DISMC, 0.035% for NISMC, and 0.044% for PI). The BSC also shows faster settling times: 0.2 ms faster than the DISMC, 0.3 ms faster than the NISMC and 0.18 ms faster than the PI controller. Furthermore, the BSC has a

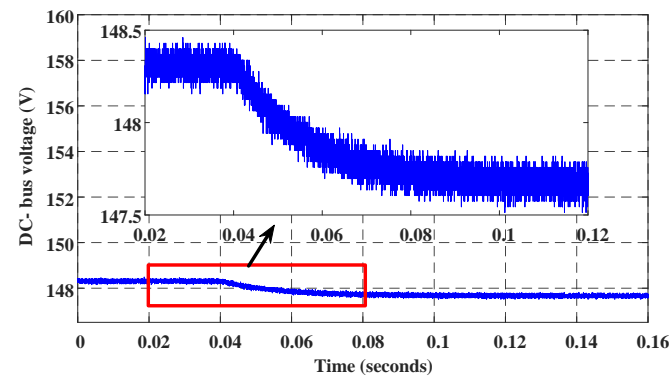


Fig. 16: Experimental waveforms with input voltage change from 50 V to 40 V using a BSC.

lower inductor current of 5 A, compared to 18 A for DISMC and 42 A for NISMC. The parametric uncertainty analysis further confirms the BSC's robustness, effectively maintains DC bus voltage near desired 340 V despite $\pm 10\%$ and $\pm 25\%$ variations in transformer turn ratio (n), inductor (L_s) , and capacitor (C_{dc}) .

The performance of the BSC is further validated through experimental tests involving an 11.764% change in reference voltage and a change of 20% in the input voltage, where it demonstrated superior performance with minimal steadystate error and overshoot. Experimental results confirmed the effectiveness of the BSC in controlling the MLDDC, with the output voltage remaining well regulated during step increases in load from 150 W to 250 W and step decreases from 250 W to 150 W. The BSC exhibited minimal chattering, small overshoots (0.23% for the increase and 0.80% for the decrease), and a steady-state error of only 0.1%. These experimental results closely match the simulation results, thus validating the effectiveness of the proposed controller. Future work will explore integrating an adaptive or integral action to further enhance performance under severe parametric uncertainty and extend the approach to other converter topologies for broader applicability.

REFERENCES

- X. Meng, Y. Jia, Q. Xu, C. Ren, X. Han, and P. Wang, "A novel intelligent nonlinear controller for dual active bridge converter with constant power loads," *IEEE Trans. Ind. Electron.*, vol. 70, pp. 2887– 2896, March 2023.
- [2] P. Prabhakaran and V. Agarwal, "Novel boost-sepic type interleaved dc-dc converter for mitigation of voltage imbalance in a low-voltage bipolar dc microgrid," *IEEE Trans. Ind. Electron.*, vol. 67, pp. 6494– 6504, August 2020.
- [3] B. Zhao, Q. Song, W. Liu, and Y. Sun, "Overview of dual-active-bridge isolated bidirectional dc-dc converter for high-frequency-link powerconversion system," *IEEE Trans. Power Electron.*, vol. 29, pp. 4091– 4106, Aug 2014.
- [4] Z. Farooq, T. Zaman, M. A. Khan, Nasimullah, S. M. Muyeen, and A. Ibeas, "Artificial neural network based adaptive control of single phase dual active bridge with finite time disturbance compensation," *IEEE Access*, vol. 7, pp. 112229–112239, Aug 2019.
- [5] T. K. Roy, M. A. Mahmud, A. M. T. Oo, M. E. Haque, K. M. Muttaqi, and N. Mendis, "Nonlinear adaptive backstepping controller design for islanded dc microgrids," *IEEE Transactions on Industry Applications*, vol. 54, no. 3, pp. 2857–2873, 2018.
- [6] T. M. Parreiras, A. P. MacHado, F. V. Amaral, G. C. Lobato, J. A. S. Brito, and B. C. Filho, "Forward dual-active-bridge solid-state transformer for a sic-based cascaded multilevel converter cell in solar applications," *IEEE Trans. Ind. Appl.*, vol. 54, pp. 6353–6363, December 2018.

- [7] Y. Xuan, X. Yang, W. Chen, T. Liu, and X. Hao, "A three-level dual-active-bridge converter with blocking capacitors for bidirectional electric vehicle charger," *IEEE Access*, vol. 7, pp. 173838–173847, Dec 2019.
- [8] M. M. Haque, P. Wolfs, S. Alahakoon, B. C. P. Sturmberg, M. Nadarajah, and F. Zare, "Dab converter with q capability for bess/ev applications to allow v2h/v2g services," *IEEE Transactions on Industry Applications*, vol. 58, no. 1, 2022.
- [9] X. Zhang, Y. Xu, A. Siddique, Y. Long, and X. Xiao, "A microprocessor resource-saving dual active bridge control for startup and restart of threestage modular solid-state transformer," *IEEE Trans. Power Del.*, vol. 35, pp. 1443–1454, Jun. 2020.
- [10] S. Y. Kim, K. Nam, H.-S. Song, and H.-G. Kim, "Fault diagnosis of a zvs dc-dc converter based on dc-link current pulse shapes," *IEEE Trans. Ind. Electron.*, vol. 55, pp. 1491–1494, March 2008.
- [11] F. Krismer and J. W. Kolar, "Accurate small-signal model for the digital control of an automotive bidirectional dual active bridge," *IEEE Trans. Ind. Electron.*, vol. 24, pp. 2756–2768, December 2009.
- [12] H. Shi, H. Wen, J. Chen, Y. Hu, L. Jiang, G. Chen, and J. Ma, "Minimum-backflow-power scheme of dab-based solid-state transformer with extended-phase-shift control," *IEEE Transactions on Industry Applications*, vol. 54, no. 4, pp. 3483–3496, 2018.
- [13] M. Yilmaz and P. T. Krein, "Review of battery charger topologies, charging power levels, and infrastructure for plug-in electric and hybrid vehicles," *IEEE Trans. Power Electron.*, vol. 28, pp. 2151–2169, May 2013
- [14] S. Inoue and H. Akagi, "A bidirectional dc-dc converter for an energy storage system with galvanic isolation," *IEEE Trans. Power Electron.*, vol. 22, pp. 2299–2306, Nov. 2007.
- [15] B. Zhao, Q. Yu, and W. Sun, "Extended-phase-shift control of isolated bidirectional dc-dc converter for power distribution in microgrid," *IEEE Trans. Power Electron.*, vol. 27, pp. 4667–4680, Nov. 2012.
- [16] H. Shi et al., "Minimum-backflow-power scheme of dab-based solid-state transformer with extended-phase-shift control," *IEEE Trans. Ind. Appl.*, vol. 54, pp. 3483–3496, Jul./Aug. 2018.
- [17] X. Liu et al., "Novel dual-phase-shift control with bidirectional inner phase shifts for a dual-active-bridge converter having low surge current and stable power control," *IEEE Trans. Power Electron.*, vol. 32, pp. 4095–4106, May. 2017.
- [18] B. Zhao, Q. Song, and W. Liu, "Efficiency characterization and optimization of isolated bidirectional dc/dc converter based on dual phase-shift control for dc distribution application," *IEEE Trans. Power Electron.*, vol. 28, pp. 1711–1727, Apr. 2013.
- [19] B. Zhao, Q. Song, W. Liu, and W. Sun, "Current-stress-optimized switching strategy of isolated bidirectional dc/dc converter with dual phase-shift control," *IEEE Trans. Ind. Electron.*, vol. 60, pp. 4458–4467, Oct. 2013.
- [20] F. Lin, X. Zhang, X. Li, C. Sun, W. Cai, and Z. Zhang, "Automatic triple phase-shift modulation for dab converter with minimized power loss," *IEEE Transactions on Industry Applications*, vol. 58, no. 3, pp. 3840– 3851, 2022
- [21] K. Wu, C. d. Silva, and W. Dunford, "Stability analysis of isolated bidirectional dual active full-bridge dc-dc converter with triple phaseshift control," *IEEE Trans. Power Electron.*, vol. 27, pp. 2007–2017, Apr. 2012.
- [22] Q. Gu, L. Yuan, J. Nie, J. Sun, and Z. Zhao, "Current stress minimization of dual-active-bridge dc-dc converter within the whole operating range," *IEEE J. Emerg. Sel. Topics Power Electron.*, vol. 7, pp. 129–142, Mar. 2019.
- [23] A. Tong, L. Hang, G. Li, X. Jiang, and S. Gao, "Modeling and analysis of a dual-active-bridge-isolated bidirectional dc/dc converter to minimize rms current with whole operating range," *IEEE Trans. Power Electron.*, vol. 33, pp. 5302–5316, Jun. 2018.
- [24] S. Inoue and H. Akagi, "A bidirectional dc-dc converter for an energy storage system with galvanic isolation," *IEEE Trans. Power Electron.*, vol. 22, pp. 2299–2306, November 2007.
- [25] L. Xue, Z. Shen, D. Boroyevich, P. Mattavelli, and D. Diaz, "Dual active bridge-based battery charger for plug-in hybrid electric vehicle with charging current containing low frequency ripple," *IEEE Trans. Power Electron.*, vol. 30, pp. 7299–7307, Dec 2015.
- [26] J. Riedel, D. G. Holmes, B. P. McGrath, and C. Teixeira, "Active suppression of selected dc bus harmonics for dual active bridge dc-dc converters," *IEEE Trans. Power Electron.*, vol. 32, pp. 8857–8867, Nov 2017.
- [27] B. Zhao, Q. Song, J. Li, Y. Wang, and W. Liu, "Modular multilevel high-frequency-link dc transformer based on dual active phase-shift principle for medium-voltage dc power distribution application," *IEEE Trans. Power Electron.*, vol. 32, pp. 1779–1791, Mar 2017.

- [28] S. Talbi, A. M. Mabwe, and A. El Hajjaji, "Control of a bidirectional dual active bridge converter for charge and discharge of a li-ion battery," in *IECON 2015 - 41st Annual Conference of the IEEE Industrial Electronics Society*, pp. 849–856, IEEE, Nov. 2015.
- [29] S. P. Engel, M. Stieneker, N. Soltau, S. Rabiee, H. Stagge, and R. W. De Doncker, "Comparison of the modular multilevel dc converter and the dual-active-bridge converter for power conversion in hvdc and mvdc grids," *IEEE Trans. Power Electron.*, vol. 30, pp. 124–137, November 2015.
- [30] N. Ullah, Z. Farooq, T. Zaman, I. Sami, A. Ibeas, K. Techato, M. S. Chowdhury, and S. M. Muyeen, "A computationally efficient robust voltage control for a single-phase dual active bridge," *Energy Reports*, vol. 6, pp. 3346–3356, December 2020.
- [31] M. R. Islam, M. A. Hossain, J. Hasan, T. K. Roy, and M. A. H. Sadi, "Double integral sliding mode controller-based bridge-type flux-coupling non-superconducting fault current limiter to protect dfig-based multi-machine power system under transient-state," *International Journal of Electrical Power & Energy Systems*, vol. 142, p. 108271, Nov. 2022.
- [32] Y. C. Jeung and D. C. Lee, "Voltage and current regulations of bidirectional isolated dual-active-bridge dc-dc converters based on a double-integral sliding mode control," *IEEE Trans. Power Electron.*, vol. 34, pp. 6937–6946, July 2019.
- [33] M. R. R. Shipon, M. S. Islam, M. R. Islam, M. A. Rahman, and M. A. Hossain, "Advanced nonlinear backstepping controller for magnetic linked dc-dc converter," in 2023 IEEE International Conference on Energy Technologies for Future Grids (ETFG), pp. 1–7, IEEE, 2023.
- [34] K. Zheng, G. Zhang, D. Zhou, J. Li, and S. Yin, "Modeling, dynamic analysis and control design of full-bridge llc resonant converters with sliding-mode and pi control scheme," *Journal of Power Electronics*, vol. 18, no. 3, pp. 766–777, 2018.
- [35] Z. Yin, L. Gong, C. Du, J. Liu, and Y. Zhong, "Sliding mode control for servo motors based on the differential evolution algorithm," *Journal* of *Power Electronics*, vol. 18, no. 1, pp. 92–102, 2018.
- [36] N. L. Díaz, A. C. Luna, J. C. Vasquez, and J. M. Guerrero, "Centralized control architecture for coordination of distributed renewable generation and energy storage in islanded ac microgrids," *IEEE Transactions on Power Electronics*, vol. 32, pp. 5202–5213, Jul. 2017.
- [37] D. C. Pandey, P. K. Behera, and M. Pattnaik, "Steady-state analysis of dual active bridge converter with single phase shift and dual phase shift modulation," in 2023 IEEE International Students' Conference on Electrical, Electronics and Computer Science (SCEECS), pp. 1–6, 2023.
- [38] H. Shi, H. Wen, J. Chen, Y. Hu, L. Jiang, and G. Chen, "Minimum-reactive-power scheme of dual-active-bridge dc-dc converter with three-level modulated phase-shift control," *IEEE Transactions on Industry Applications*, vol. 53, no. 6, pp. 5573–5586, 2017.
- [39] M. A. Hossain, M. R. Islam, M. Y. U. Haque, J. Hasan, T. K. Roy, and M. A. H. Sadi, "Protecting dfig-based multi-machine power system under transient-state by nonlinear adaptive backstepping controller-based capacitive bfcl," *IET Generation, Transmission & Distribution*, vol. 16, pp. 4528–4548, Nov 2022.



Md. Rezaur Rahman Shipon received the B.Sc. and is currently pursuing the M.Sc. degree in Electrical and Electronic Engineering (EEE) from the Rajshahi University of Engineering and Technology (RUET), Rajshahi, Bangladesh. He was a lecturer at Varendra University, Bangladesh, from November 2021 to March 2024. He also worked as an Assistant Engineer with the Bangladesh Industrial Technical Assistance Centre (BITAC). He is currently working as an Assistant Engineer with Northern Electricity Supply PLC (NESCO). His research interests in-

clude smart grids, microgrid systems, power electronics, renewable energy systems, and power system control.



Md. Rashidul Islam received the B.Sc. and M.Sc. degrees in Electrical and Electronic Engineering (EEE) from the Rajshahi University of Engineering and Technology (RUET), Rajshahi, Bangladesh, in 2013 and 2017, respectively. Currently he is pursuing his PhD with School of Electrical and Data Engineering at University of Technology Sydney (UTS), Australia. He is also an Assistant Professor (on leave) with the Department of EEE, RUET. His research interests include smart grid, cybersecurity, nonlinear controller design and applications on re-

newable energy systems, the applications of power electronics in renewable energy and microgrid systems. He received the University Gold Medal Award from the RUET. He also received the Prime Minister Gold Medal Award.



Md. Shazarul Islam received his B.Sc. degree in Electrical and Electronic Engineering from Rajshahi University of Engineering and Technology, Rajshahi, Bangladesh. His research focuses on power electronics and VLSI design, with a recent publication on magnetic link DC converters. He is also deeply interested in digital verification and hardware codesign.



Md. Shahan Sarker is currently pursuing the M.Sc. degree in Electrical and Electronic Engineering at the Bangladesh University of Engineering and Technology (BUET), with a specialization in Power Systems and Electrical Energy. He received the B.Sc. degree in Electrical and Electronic Engineering from Rajshahi University of Engineering and Technology (RUET), Rajshahi, Bangladesh. His research interests include smart grids, cybersecurity, nonlinear controller design, and their applications in renewable energy systems. He is also interested in

the integration of power electronics into renewable energy and microgrid systems. Additionally, his work focuses on the application of optimization algorithms, machine learning (ML), deep learning (DL), and reinforcement learning (RL) in electrical engineering. He is passionate about research and actively seeks opportunities to contribute to advanced research laboratories and pursue higher studies in this field.



Md. Ashib Rahman (Member, IEEE) received his B.Sc. and Ph.D. degrees from Rajshahi University of Engineering and Technology, Bangladesh, and the University of Wollongong (UOW), Australia, in 2014 and 2021, respectively, both in electrical engineering. He has worked as an Associate Research Fellow on Australian Research Council Discovery Project at UOW in 2022. He has served as a Power Systems Engineer at APD Engineering, Melbourne, Australia in 2023. Currently, he is seconded to Australian Energy Market Operator (AEMO) as a

System Design Engineer. His work interests include solid-state transformers, grid integration of renewables, dynamic control and protection of commercial inverters, NEM network modelling and commissioning and hold point testing of renewable plants.



Md. Alamgir Hossain (Senior Member, IEEE) received the B.Sc. (Eng.) degree (Hons.) in Electrical and Electronic Engineering (EEE) from Dhaka University of Engineering and Technology (DUET), Bangladesh, in 2012, and the M.E. and Ph.D. degrees in Electrical Engineering from the University of New South Wales (UNSW), Australia, in 2016 and 2019, respectively.

He is currently a Senior Lecturer in Electrical and Electronic Engineering at the University of Southern Queensland, Toowoomba, Australia. Previously, he

was a Senior Research Fellow at the Queensland Micro-and Nano-Technology Centre, Griffith University, Australia, where he built Australia's first Hydrogen DC Microgrid Laboratory for research and industry-standard purposes, funded by the Blue Economy Cooperative Research Centre. Before joining Griffith University, he was a full-time Postdoctoral Research Associate at UNSW for one and a half years. He has been awarded several prestigious scholarships, including the University International Postgraduate Award, the University College Postgraduate Research Scholarship, and the UNSW Canberra-Study Canberra Scholarship. He has published more than 110 high-impact research articles and has received several awards, including Best Research Presenter (poster), Second-Best Presenter at UNSW Canberra Research Days, Top Peer Reviewer, Outstanding Reviewer from Elsevier, and the Prime Minister and President Gold Medals. His fields of interest include renewable energy integration, energy management, power generation prediction, optimal operation, microgrids, control systems, battery energy, hydrogen fuel cells and electrolysers, and smart grids.



Waqas Hassan (Senior Member, IEEE) received the bachelor's (Hons.) and master's degrees in electrical engineering from the University of Engineering and Technology, Taxila, Pakistan, in 2010 and 2014, respectively, and the Ph.D. degree in electrical engineering from The University of Sydney, Sydney, NSW, Australia, in 2020. He is currently a Senior Lecturer with the School of Engineering, University of Tasmania, Hobart, TAS, Australia. Prior to his current position, he was a Senior Engineer with Regal Rexnord Corporation, Melbourne, VIC, Aus-

tralia, where he worked on next-generation motor drives. He has over ten years of experience in academic, research, and industry in the power and energy sector. His recent works have been featured by the IEEE Industrial Electronics Society and IET Renewable Power Generation. His research interests include designing and developing power electronics technologies and products for various applications, solar photovoltaic power systems, renewable energy systems, battery storage and grid integration, DC microgrids, and motor drives.